# Orienting anisometric pores in ferroelectrics: Piezoelectric property engineering through local electric field distributions

J. Schultheiß<sup>1</sup>, J. I. Roscow<sup>2,\*</sup>, and J. Koruza<sup>1</sup>

<sup>1</sup> Institute of Materials Science, Technische Universität Darmstadt, Alarich-Weiss-Straße 2, 64287, Darmstadt, Germany

<sup>2</sup> Materials and Structures Centre, Department of Mechanical Engineering, University of Bath, Claverton Down, Bath, BA2 7AY, UK

\* Corresponding author

#### **Abstract**

Ferroelectrics are a technologically important class of materials, used in actuators, sensors, transducers, and memory devices. Introducing porosity into these materials offers a method of tuning functional properties for certain applications, such as piezo-and pyroelectric sensors and energy harvesters. However, the effect of porosity on the polarization switching behaviour of ferroelectrics, which is the fundamental physical process determining their functional properties, remains poorly understood. In part, this is due to the complex effects of porous structure on the local electric field distributions within these materials. To this end, freeze cast porous lead zirconate titanate ceramics were fabricated with highly oriented, anisometric pores and an overall porosity of 34 vol.%. Samples were sectioned at different angles relative to the freezing direction and the effect of pore angle on the switching behaviour was tracked by simultaneously measuring the temporal polarization and strain responses of the materials to high voltage pulses. Finite element modelling was used to assess the effect of the pore structure on the local electric field distributions within the material, providing insight into the experimental observations.

It is shown that increasing the pore angle relative to the applied electric field direction decreases the local electric field, resulting in a reduced domain wall dynamic and a broadening of the distribution of switching times. Excellent longitudinal piezoelectric  $(d_{33} = 630 \text{ pm/V})$  and strain responses  $(S_{bip} = 0.25\% \text{ and } S_{neg} = 0.13\%$ , respectively), comparable to the dense material  $(d_{33} = 648 \text{ pm/V}, S_{bip} = 0.31\% \text{ and } S_{neg} = 0.16\%)$ , were found in the PZT with anisometric pores aligned with the poling axis. Orienting the pores perpendicular to the poling axis resulted in the largest reductions in the

effective permittivity ( $\varepsilon_{33}^{\sigma}$ = 200 compared to  $\varepsilon_{33}^{\sigma}$  = 4100 for the dense at 1 kHz), yielding the highest piezoelectric voltage coefficient ( $g_{33}$  = 216 x 10<sup>-3</sup> Vm/N) and energy harvesting figure of merit ( $d_{33}g_{33}$  = 73 x 10<sup>-12</sup> m²/N). These results demonstrate that a wide range of application-specific properties can be achieved by careful control of the porous microstructure. This work provides a new understanding of the interplay between the local electric field distribution and polarization reversal in porous ferroelectrics, which is an important step towards further improving the properties of this promising class of materials for sensing, energy harvesting, and low-force actuators.

#### 1. Introduction

Piezo- and ferroelectric materials find application in numerous electronic devices and are enabling components for the development of new technologies. In order to achieve high performance, porosity is usually considered undesirable, reducing the piezoelectric and dielectric response, enhancing electrical fatigue [1], and degrading mechanical strength [2]. The targeted introduction of porosity into ferroelectric ceramics, however, offers a facile method for tuning the piezoelectric, pyroelectric, dielectric and mechanical properties, enabling the development of materials with superior application-specific figures of merit [3]. For example, the introduction of porosity can lead to a decoupling of longitudinal and transverse piezoelectric properties  $(d_{33}$  and  $d_{31}$ , respectively), which improves the hydrostatic piezoelectric strain  $(d_h =$  $d_{33}+2d_{31}$ ) and hydrostatic voltage coefficient ( $g_h=d_h/\varepsilon_{33}^{\sigma}$ ) [4]. This has led to interest in the use of porous ferroelectrics for hydrophones [5-7], thermal sensors [8,9] and piezo- and pyroelectric energy harvesters [10-12]. A further benefit for hydrophones and medical ultrasound devices is the improved acoustic impedance matching between water/human tissue and the porous ceramic caused by the reduction in density of the ferroelectric with increasing pore fractions [4,13].

Porous ferroelectrics with isometric pores have been extensively studied due to relative ease of manufacture using, for example, the coral replica [4] or the burned out polymer spheres (BURPS) approach [14]. Additionally, it has been demonstrated that the longitudinal piezoelectric coefficient [15] can be further improved if anisometric pores are introduced and oriented in the direction of the applied poling field. For example, the piezoelectric strain coefficients approach values of the dense samples, while the effective permittivity at constant stress ( $\varepsilon_{33}^{\sigma}$ ) of the material is reduced [10,13,15,16]. Reducing  $\varepsilon_{33}^{\sigma}$  whilst maintaining a high  $d_{33}$  leads to increases in the piezoelectric voltage coefficient [17]:

$$g_{33}=d_{33}/\varepsilon_{33}^{\sigma},$$
 Equation 1

and longitudinal piezoelectric energy harvesting figure of merit,  $d_{33}g_{33}$  [18]. The introduction of porosity does, however, reduce the elastic modulus [19] and mechanical compressive strength [20] of polycrystalline ceramics. Whilst this tends to make them unsuitable for actuation applications with high blocking force requirements, the decrease in elastic modulus can be beneficial for sensing and harvesting applications,

where mechanical impedance matching between the energy source and the active material is required [21]. In addition, the elastic stiffness and compressive strength can be increased by orienting anisometric pores to the loading direction, compared to ceramics with isometric pore structures. [22] While the correlation between porosity and elastic stiffness is well studied for polycrystalline ceramic materials [23], few studies link porosity to the local electric field distribution and functional ferroelectric properties.

The response of porous ferroelectric ceramics to an external electric field, for example during poling or large signal measurements, predominantly depends on the local distribution of the applied electric field. The electric field varies locally in dense polycrystalline materials due to anisotropy of the dielectric tensor and the random orientation of the grains [24,25]. Porous materials exhibit an even broader distribution due to the large differences in permittivity between the ferroelectric matrix and the pores [26-31]. In this context, the impact of the total porosity, pore size, shape, and orientation of anisometric pores on the local electric field distribution has been studied using finite element (FE) simulations [26]. While the distribution of the local electric fields was independent of the pore size, it was found to be sensitive to the total porosity, anisometric shape, and the orientation of the pores. Median values of the local electric field were reduced and broadening of the distribution was reported for increased isometric pore volume fraction [27,28,32], resulting in tilted polarization hysteresis loops for porous materials [27,33]. The impact of pore fraction on polarization reversal was studied in more detail by first-order reversal curve analysis. A sharp transition was found for a dense material and a broad transition was reported for a porous material with isometric pores [30]. The impact of isometric pore sizes on switching properties was investigated for a Pb( $Zr_{0.53}Ti_{0.47}$ )O<sub>3</sub> material with pore sizes of 1 µm and 8 µm [34]. A dramatic change in the switching behaviour was reported, expressed for example by a doubling of the remanent polarization, which is in disagreement to theoretical predictions. However, it should be mentioned that the change in pore size was accompanied by a change in grain size [34], which also alters the switching behaviour of ferroelectric/ferroelastic ceramic materials [35]. For anisometric pores oriented parallel to the electric field, a more homogenized and localized distribution of switching times was found, while for anisometric pores oriented perpendicular to the electric field the distribution of switching times broadened [30].

Whereas most of the studies of porous ferroelectrics have focussed on the interplay between the complex local electric field distribution and the switching behaviour, ferroelectric/ferroelastic domains, which determine the polarization reversal [36], are usually neglected. It has recently been shown that a deeper understanding of polarization reversal process can be achieved by simultaneously measuring the dynamic polarization and strain response of a ferroelectric material [37,38]. In this context, three regimes of polarization reversal can be distinguished in polycrystalline ferroelectrics. Starting from the poled state, which is characterized by the presence of mainly non-180° domain walls [39], an electric field pulse is applied antiparallel to the poling direction. The first regime is described by rapid movement of non-180° domain walls triggered by the applied electric field [40] and internal mechanical stresses [41]. In the second regime (main switching phase), where up to 80% of the polarization reversal occurs, strain-free 180° [42] and synchronized non-180° [43] switching events have been suggested. The saturation of the switching process (third regime) is dominated by slow creep-like movement of non-180° domain walls [44]. It has been recently demonstrated that these switching phases are considerably influenced by the crystallographic structure [45], impacting the activation fields and domain wall dynamics. Among the identified parameters influencing the switching behaviour was also the distribution of the local electric fields, which is expected to change even more when porosity is intentionally introduced into a material.

The aim of this work is to explore the influence of the orientation of anisometric pores on the polarization switching behaviour of porous ferroelectrics. Therefore, freeze cast Pb(Zr,Ti)O<sub>3</sub> (PZT) materials with anisometric pores oriented at well-defined angles with respect to the electric field were fabricated (66% relative density). The switching behaviour was investigated by measuring the dynamic polarization and strain response simultaneously. The inhomogeneous distributions of the electric field, calculated by FE simulations, are discussed in context of the material's polarization reversal and functional properties. Dense PZT (97% relative density) with a similar grain size to the freeze cast samples was fabricated to provide comparison with the switching dynamics and functional properties of the porous samples. Finally, guidelines for the enhancement of individual functional properties by pore orientation are provided.

## 2. Experimental

## A. Materials fabrication and characterization

Porous PZT samples with highly oriented, anisometric pores were fabricated using the freeze casting method. Commercial PZT powder (NCE55, Noliac, Denmark) was ball milled in ethanol with zirconia milling media for 48 h to break up agglomerates formed during production, prior to drying and regrinding, resulting in a mean particle size of ~1 µm. A suspension with 30 vol.% PZT powder in deionized water with 1 wt.% binder (polyethylene glycol,  $m_w = 100,000$ , Sigma-Aldrich, UK) and 0.5 wt.% dispersant (polyacrylic acid, Sigma-Aldrich, UK) was mixed for 24 h on a rotary ball mill before freeze casting in open cylindrical silicone moulds on an aluminium heat sink in a custom built, single-sided freeze casting set up [12]. The heat sink was cooled with liquid nitrogen to -40 °C at an initial rate of -6 °C/s to initiate directional freezing of the suspension. After freezing, the samples were freeze dried for 24 h to remove the ice. Subsequently the green bodies were sintered at 1200 °C for two hours with a dwell stage at 400 °C for 2 h to remove organic additives. To prevent lead loss during sintering, additional PZT powder was added to the crucible with a fitted lid. The heating and cooling rates during sintering were 1 °C/min. After sintering, individual samples were cut at least 6 mm from the base of the freeze cast bodies (i.e., the side from which freezing was initiated) at different angles ( $\theta = 0^{\circ}, 22.5^{\circ}, 45^{\circ}, 67.5^{\circ}, 90^{\circ}$ ) with respect to the freezing direction. These also represent the angle between the main axis of the pore channels and the direction of the applied electric field.

A dense PZT sample with the same chemical composition was produced for comparison. The starting powder was mixed with 4 wt.% binder (polyethylene glycol,  $m_W = 100,000$ , Sigma-Aldrich, UK) in deionized water in a ball mill for 24 h. The suspension was dried, ground, and sieved through a 150  $\mu$ m mesh. Green pellets were formed by uniaxially pressing the powder (220 MPa) into pellets with a diameter of 13 mm. The pellets were sintered under the same conditions as the freeze cast samples.

The density of the samples was measured using the Archimedes method. Microstructures were investigated using scanning electron microscopy (SEM, JSM-6480LV, Jeol, USA). Dense and porous samples were prepared by standard grinding and polishing methods (EcoMet 250 Pro, Buehler, UK) and thermally etched at 900 °C for 1.5 h to reveal the grain boundaries. For the SEM images used for the FE modelling, a porous sample was mounted in resin (SpeciFix, Struers, UK) prior to polishing to

yield sufficient contrast between phases for effective image binarization (details in Section 2D). The grain size was measured by the linear intercept method from micrographs taken from three different areas of each sample, with over 300 grains measured in total per sample. A numerical multiplication factor of 1.56 was employed [46]. X-ray diffraction (XRD) of the sintered samples was performed using a X-Ray diffractometer (D8 Advance, Bruker, Germany) in Bragg-Bretano geometry and Cu  $K\alpha$  radiation ( $\lambda$  = 0.15418 nm). The thickness of the disc- and bar-shaped samples for electrical measurements was in the range of 1.4–1.7 mm, while the area was 30–40 mm². The samples' top and bottom surfaces were painted with silver paste (Gwent Group, Pontypool, UK), which was heat treated at 500°C to form the electrodes.

## B. Small-signal measurements

Prior to small-signal measurements, the samples were poled at room temperature under an electric field of 1.5 kV/mm for 10 s and were allowed to relax for one day. Temperature- and frequency-dependent relative permittivity was measured at 1 kHz, with a voltage of 1 V and a heating rate of 2 °C/min using an impedance analyser 4192A (Hewlett Packard Corporation, CA, USA). Field-dependent small signal permittivity was measured using a commercial system (TF2000, aix-ACCT Systems, Aachen, Germany), whereby a small signal waveform (triangular waveform, 1.4 V/mm, 100 Hz) was modulated on a large signal waveform (triangular waveform, 2 kV/mm, 0.01 Hz). Small-signal  $d_{33}$  values were collected by a Berlincourt meter (Piezotest PM 300, Singapore) with a dynamic force of 0.25 N at a frequency of 110 Hz under an applied static force of 2 N.

# C. Large-signal measurements

The HV response was characterized by hysteresis loop measurements and pulse switching experiments. Prior to the measurement, all samples were annealed at 500 °C (heating/cooling rate 2 °C/min) and the pores were filled with silicone oil under vacuum to prevent dielectric breakdown. Next, the samples were electrically cycled 20 times using a bipolar field (0.5 Hz, 1.5 kV/mm) to remove any unstable electrical contributions.

# **Hysteresis measurements**

Field-dependent polarization and strain loops were recorded at electric fields in the range of 1.0–4.0 kV/mm and 0.1 Hz using a triangular waveform. The polarization was

recorded by a modified Sawyer-Tower circuit, while the displacement was measured by an optical displacement sensor (D63, Philtec Inc., MD, USA). The HV source (Trek Model 20/20C, NY, USA) was controlled remotely by a LabView program.

# **Pulse switching**

The samples were poled with 1.5 kV/mm for 10 s using a high voltage (HV) source. After poling, the samples were allowed to relax for 100 s. HV switching pulses with a rise time of 115 ns were provided by the combination of a 2  $\mu$ F capacitor and a commercial fast HV transistor switch (HTS 41-06-GSM, Behlke GmbH, Germany), triggered by a function generator (Agilent 33220A, CA, USA). The polarization was measured using a modified Sawyer-Tower circuit. An optical displacement sensor was used simultaneously to record the macroscopic dimensions of the sample in the direction of the applied electric field l(t), which allowed calculation of the strain of the sample  $\epsilon = (l(t) - l_{init})/l_{init}$ , where  $l_{init}$  is the dimension of the sample after poling. The switched polarization,  $\Delta P(t)$ , was isolated from other contributions (dielectric displacement and integrated leakage current) by applying a field sequence during the measurement, which contains a switching and a reference part [47]. A detailed description of the experimental setup and the measurement sequence for the dynamic polarization and strain switching measurements is given elsewhere [37].

In order to ensure that the pulse switching experiment did not irreversibly impact the material, a bipolar polarization and strain loop was recorded before and after each experiment (triangular waveform, 3 kV/mm, 0.1 Hz).

## D. Finite element simulations

The electric field distributions within dense and porous PZT microstructures were simulated using Ansys APDL v18.1 to solve Gauss' equation by assuming the material to behave as a composite dielectric. The input relative permittivity values used were  $\varepsilon_r=1500$  for the PZT phase (experimentally determined at 1.5 kV/mm, Figure S1), and  $\varepsilon_r=2.3$  for the non-PZT phase to represent the dielectric properties of silicone oil, i.e., the medium in which the samples were measured experimentally. An electric field of 1.5 kV/mm was applied across the thickness to obtain local electric fields within PZT elements. The geometries of the models were obtained from SEM micrographs. Porous samples were mounted in resin and polished to achieve sufficient contrast between the porous and ceramic phases (see Section 2A). The micrographs (100 µm

x 100 µm) were binarized and converted into a meshed Ansys model using Matlab (500 x 500 and 400 x 400 equiaxed elements for dense and porous samples, respectively). The  $\theta=0^\circ$  geometry was generated from an SEM image of the longitudinal section of a sample, and the  $\theta=90^\circ$  geometry generated from the cross section. The latter was then also used to form the geometries of the other pore angles ( $\theta=22.5^\circ,45^\circ,67.5^\circ$ ) by applying a stretch ratio,  $1/\sin\theta$ , in one direction to achieve a representative cross-sectional geometry. The stretch ratio is related to the change in cross sectional aspect ratio due to different slice angles (details are provided in Figure S2).

#### 3. Results

## A. Crystallography and Microstructure

XRD patterns of a dense and a freeze cast sample are displayed in Figure S3. All peaks can be assigned to a perovskite phase. The investigated PZT composition is on the tetragonal side of the MPB, since the 111 peak is a singlet and a small splitting can be observed in the 200 peaks. The densities obtained by the Archimedes method were 66% and 97% of the theoretical density for the freeze cast and the dense sample, respectively. SEM micrographs of both samples are displayed in Figure 1. As highlighted in Figure 1a and b, the dense sample contains only intrinsic porosity. On the other hand, a preferred orientation of the anisometric pores can be clearly observed for the freeze cast samples, as shown in Figure 1c. In the framework of the connectivity concept for composite materials introduced by Newnham et al. [17], the freeze cast materials can be described as having a 3-1 type structure, where the ferroelectric phase has continuous connectivity in three dimensions, with one dimensional pore channels aligned in the direction of freezing. The pore channels of the freeze cast sample are displayed in the inset in Figure 1c. The freeze cast samples exhibit excellent densification within the PZT phase with very little intergranular porosity, which is similar to a dense sample. A comparable grain size of 3.1 µm and 3.6 µm were found for the dense and the freeze cast sample, respectively. PZT samples within this grain size range [35,48] are expected to have a banded domain structure, which contains 180° and non-180° domain walls [49].

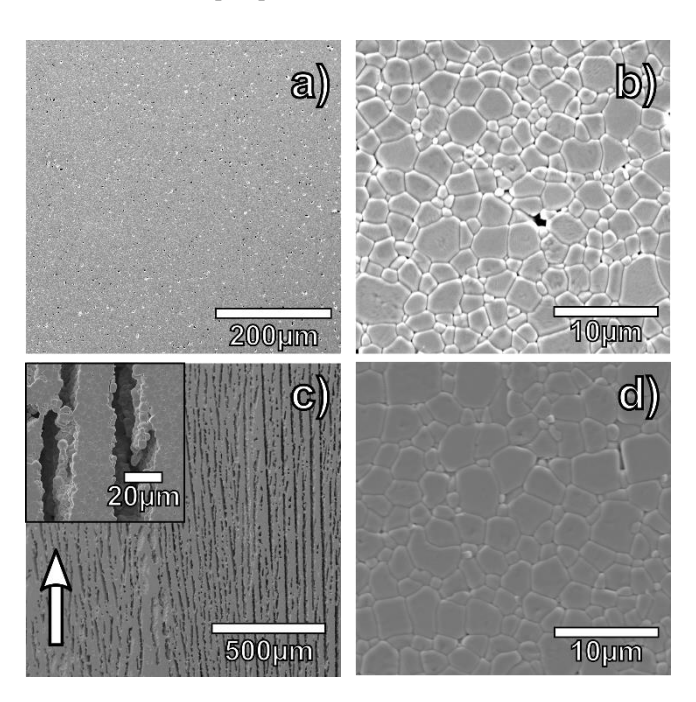


Figure 1: Microstructures of dense PZT (a, b), and freeze cast porous PZT with 34 vol.% porosity (c, d). The arrow in c) indicates the freezing direction. The inset in c) displays the oriented anisometric pore channels within the PZT. The PZT phase is magnified in d).

#### B. Local electric field distribution

The impact of the pore orientation on the individual components of the local electric field was determined using two-dimensional FE simulations, as displayed in Figure 2. Binary images converted from SEM images of freeze cast samples (Figure 1c and d) were transferred into meshed geometries (first row in Figure 2a). The z-component of the local electric field,  $E_{loc,z}$ , is visualized in the second row of Figure 2a. The distributions of the local electric field value with respect to the externally applied field, E, are plotted for samples with different pore orientation angles in Figure 2b and for a dense material in Figure 2c. The frequencies have been normalised so that the integral under each curve is unity. It was found that the z-component of the local electric field of porous samples had a much wider distribution compared to the dense sample with a sharp homogeneous distribution centred close to the applied electric field, i.e.,  $E_{loc,z}/E=1$ . In addition, the local electric field distribution shifted towards lower fields when the pore orientation angle increased. Also, the broadness of the local electric field distribution increased with increased pore orientation angle. It should be highlighted that the inhomogeneous field distributions in these simulations were a result of the difference in the permittivity of the ferroelectric phase and the pores, and their geometrical arrangement. Other effects impacting the distribution of the local electric field in the ferroelectric phase, such as the distribution of c-axes due to a random orientation of grains, as described elsewhere [50], and domain structure were not considered.

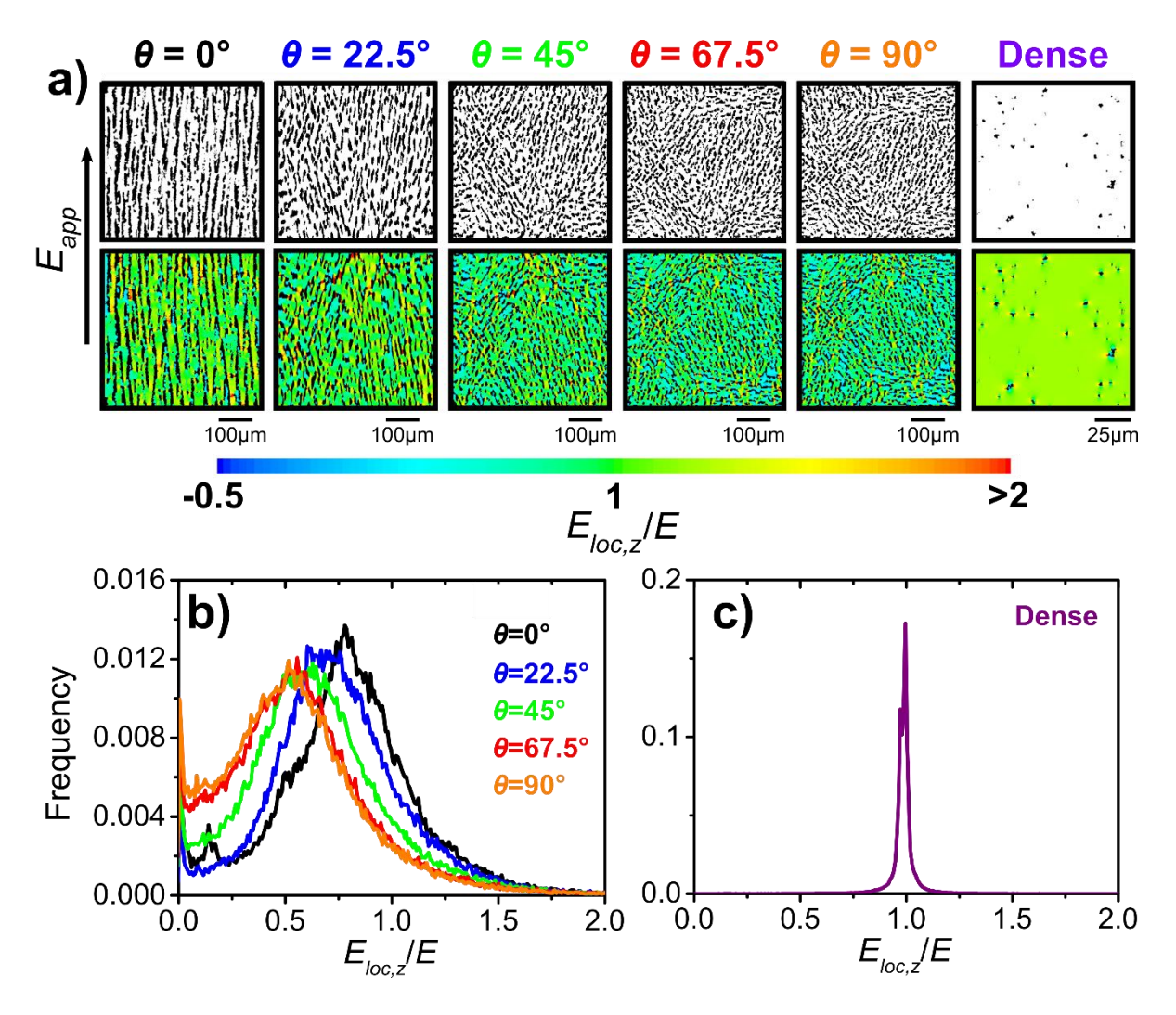


Figure 2: a) Binary images, in which the pores are black and the PZT phase is white, converted from SEM micrographs into meshed geometry and resulting contour plots for the local field distribution within the PZT phase. The different colours indicate the value of the local electric field in z-direction, E<sub>loc,z</sub>. Local electric field distributions are displayed for samples with different orientation angles in b). The local electric field distribution for the dense sample is displayed for comparison in c).

# C. Large- and small-signal measurements

Large-signal macroscopic polarization and strain hysteresis loops under the application of a bipolar triangular electric field of 1.5 kV/mm (0.1 Hz) are displayed in Figure 3. Parameters characterizing the hysteretic behaviour are summarized in Table 1. The coercive field (electric field where  $P=0~\mu\text{C/cm}^2$ ) increased, while the remanent polarization decreased with increasing pore orientation angle  $\theta$ . Comparing the  $\theta=0^\circ$  and  $\theta=90^\circ$  samples, the coercive field increased by 12%, while the remanent polarization reduced by 65% at the higher pore angle. A similar behaviour was

observed for the electric field-induced strain response of the materials. Interestingly, the bipolar and negative strain of the  $\theta=0^\circ$  sample  $(S_{bip}^{\theta=0^\circ}=0.25\%$  and  $S_{neg}^{\theta=0^\circ}=0.13\%)$  were in the range of the dense material  $(S_{bip}^{dense}=0.31\%$  and  $S_{neg}^{dense}=0.16\%)$ , while the values were about 55% lower for the  $\theta=90^\circ$  sample  $(S_{bip}^{\theta=90^\circ}=0.12\%)$  and  $S_{neg}^{\theta=90^\circ}=0.06\%)$ . The similarity between the strain response of the  $\theta=0^\circ$  porous sample and the dense material indicate potential for porous ferroelectrics as transmitters or lightweight actuators. However, these would exhibit a reduced blocking force compared to their dense counterparts due to the decrease in the elastic modulus that occurs when porosity is introduced [23]. While these materials would be unsuitable for actuating large objects [51], they may be of used for low-force actuating applications [52].

The shapes of the P(E) loops (Figure 3a and c) were quantified by the squareness ratio  $R_{Sq}[53]$ :

$$R_{Sq} = \frac{P_r}{P_{Sqt}} + \frac{P_{1.1E_C}}{P_r}$$
 Equation 2

Here  $P_{1.1Ec}$  is the polarization taken at  $1.1E_c$  on loops measured at 1.5 kV/mm and  $P_{Sat}$  is the polarization at 1.5 kV/mm. As displayed in Table 1, the squareness ratio decreased with increasing pore orientation angle and values of  $R_{Sq}^{\theta=0^{\circ}}=1.19$  and  $R_{Sq}^{\theta=90^{\circ}}=1.02$  were found for the  $\theta=0^{\circ}$  and the  $\theta=90^{\circ}$  samples, respectively. All values were well below  $R_{Sq}=2$ , which is the theoretical value for a defect-free single crystalline material [53]. The broadening of the hysteresis loop is also manifested by the sharpness of the S(E) curve at the maximum negative strain (Figure 3b). The curve was relatively sharp for the  $\theta=0^{\circ}$  sample, however, it became broader and more dispersive for the  $\theta=90^{\circ}$  sample. The squareness ratio of the dense sample  $(R_{Sq}^{dense}=1.14)$  was slightly lower than that of the  $\theta=0^{\circ}$  sample.

The small-signal piezoelectric and dielectric properties were also affected by the pore orientation angle. A  $d_{33}^{\theta=0^{\circ}}=630$  pm/V was measured for the  $\theta=0^{\circ}$  sample, while a 46% reduced value ( $d_{33}^{\theta=90^{\circ}}=338$  pm/V) was found for the  $\theta=90^{\circ}$  sample. The  $d_{33}^{\theta=0^{\circ}}$  was comparable to the piezoelectric response of the dense material ( $d_{33}^{dense}=648$  pm/V). As displayed in Table 1, the dielectric response of the material also decreased with increasing angle  $\theta$ . The calculated piezoelectric voltage coefficient,  $g_{33}$  (Equation 1), is displayed in Table 1. The lowest value ( $g_{33}^{dense}=18\cdot10^{-3}$  Vm/N) was found for

the dense material. The  $\theta=0^\circ$  sample exhibits a value of  $g_{33}^{\theta=0^\circ}=41\cdot 10^{-3}$  Vm/N, while a value of  $g_{33}^{\theta=90^\circ}=216\cdot 10^{-3}$  Vm/N was found for the  $\theta=90^\circ$  sample. The energy harvesting figure of merit  $d_{33}\cdot g_{33}$  was increased by a factor of 2.8 by rotating the pore angle from  $\theta=0^\circ$  to  $\theta=90^\circ$  (Table 1), and by a factor of 6.1 compared to the dense PZT. These increases in figures of merit for sensing  $(g_{33})$  and energy harvesting  $(d_{33}g_{33})$  demonstrate that for the investigated materials, the decrease in low signal permittivity with increasing pore angle was more dominant than the decrease in  $d_{33}$ .

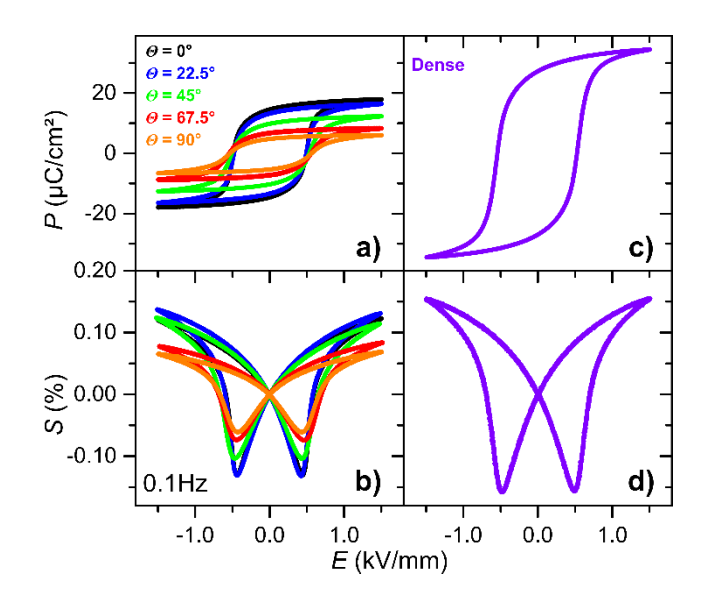


Figure 3: Large-signal a) polarization, P, and b) strain, S, hysteresis loops as a function of the electric field, E, of freeze cast porous PZT polycrystalline materials with anisometric pores oriented at different angle  $\theta$  to the external electric field (porosity 34%). A measurement of a dense sample is displayed in c) and d) for comparison.

Table 1: Large-signal properties (coercive field,  $E_c$ , remanent polarization,  $P_r$ , bipolar strain,  $S_{bip}$ , negative strain,  $S_{neg}$ ; all measured at 0.1 Hz and 1.5 kV/mm), small-signal properties (piezoelectric coefficient,  $d_{33}$ , maximum permittivity at ferroelectric-paraelectric phase transition temperature ( $T_c$ ) and at room temperature (RT),  $\varepsilon_{33}^{\sigma}$ ), and application relevant figures of merit (piezoelectric voltage coefficient,  $g_{33}$  and energy harvesting figure of merit  $d_{33}g_{33}$ ) for PZT samples with anisometric pores aligned at different angles  $\theta$  to the external electric field (porosity 34%). The respective values of a dense sample are displayed for comparison.

Sampl	Ec	$P_r$	$S_{bip}$	S <sub>neg</sub>	$R_{Sq}$	<b>d</b> 33	$arepsilon_{33}^{\sigma}$ .	$arepsilon_{33}^{\sigma}$ .	$g_{33}$	$d_{33}g_{33}$
е	(kV/m	(µC/c	(%)	(%)	(%)	(pm/V	$10^{3}$	$10^{3}$	(at	(at
	m)	m²)				)	(at $T_c$ ,	(at	RT,	RT,
							1	RT, 1	10 <sup>-3</sup>	10 <sup>-12</sup>
							kHz)	kHz)	Vm/N)	m²/N)
$\theta = 0^{\circ}$	0.49	14.5	0.25	0.13	1.19	630	12.5	1.7	41	26
θ	0.48	13.2	0.27	0.13	1.13	639	11.7	1.5	48	31
= 22.5°										
θ	0.52	10.0	0.22	0.10	1.13	565	8.8	0.8	78	44
= 45°										
θ	0.55	6.9	0.15	0.07	1.09	411	6.1	0.3	139	57
= 67.5°										
θ	0.55	5.0	0.12	0.06	1.02	338	5.0	0.2	216	73
= 90°										
Dens	0.54	27.3	0.31	0.16	1.14	648	20.8	4.1	18	12
е										

# D. Field-dependency of large-signal measurements

Although the hysteresis loops in Figure 3 appear well saturated, the properties of the investigated porous materials strongly depend on the amplitude of the applied electric field. The experimentally obtained correlations between the field amplitude and the polarization and strain loops are displayed in Figure 4a for the  $\theta=0^\circ$ ,  $\theta=45^\circ$ , and  $\theta=90^\circ$  samples. For the latter two angles, it can be observed that the polarization and strain loops further open if the electric field is increased. The field-dependency for the dense sample is shown in Figure S4 for comparison.

The dependence of the remanent polarization on the applied field is displayed in Figure 4b. The remanent polarization of a porous material can be quantified by Equation 3 [32,54]:

$$P_r = d_P \cdot P_r^0 (1 - \nu_p)$$
 Equation 3

The remanent polarization depends on the porosity volume fraction,  $v_p$ , and the remanent polarization of a dense counterpart,  $P_r^0$ . Equation 3 assumes that there is no

change in the intrinsic or extrinsic ferroelectric contributions to polarization with the introduction of high volumes of porosity. A depolarization factor,  $d_P$ , was introduced into Equation 3 to account for the disparity between experimental observations and a simple volume fraction relationship for the effect of porosity on remanent polarization [32], whereby the depolarization factor experimentally quantifies the volume fraction of the active material. The limiting remanent polarization for a specific pore volume fraction is predicted by Equation 3 to occur when  $d_P = 1$ . The value obtained from Equation 3 for the investigated porous samples ( $d_P = 1$  and  $v_P = 0.34$ ) is 20  $\mu$ C/cm², which is displayed in Figure 4b by the dashed red line.

Although the  $\theta = 0^{\circ}$  sample approached the theoretical polarization limit at relatively low field amplitudes, as displayed in Figure 4b, the remanent polarization did not saturate within the experimental field range for the  $\theta = 90^{\circ}$  sample. The  $\theta = 0^{\circ}$  sample could not be measured at applied fields greater than E = 2.5 kV/mm due to dielectric breakdown. The remanent polarization of the  $\theta = 45^{\circ}$  sample was doubled, as can be seen in Figure 4b by comparing the results at 1.0 kV/mm and 4.0 kV/mm. Within the same electric field range the remanent polarization of a dense counterpart increased by only 20%. This experimental observation for the porous materials is related to the distribution of the local electric field, which broadens and on average reduces with increasing pore orientation angle, as demonstrated by the FE model (Figure 2b). Using the model to understand this behaviour, we can consider the fraction of the active material ( $f_{act}$ ) as the fraction that is subject to a local electric field exceeding a threshold value. For arguments sake, we have used the coercive field of the  $\theta=0^{\circ}$  sample at 1.5 kV/mm, i.e., 0.49 kV/mm, as the threshold field. As a consequence of the local distribution of the electric field, a higher volume fraction of the material can be activated if the externally applied electric field is increased (Figure 4c). The results are in a reasonable qualitative agreement with the experimental results, as an increase of the externally applied electric field causes a quick saturation for the  $\theta = 0^{\circ}$  sample, while the saturation is delayed for the  $\theta = 90^{\circ}$  sample, indicating that this polarization field response results largely from the porous microstructure.

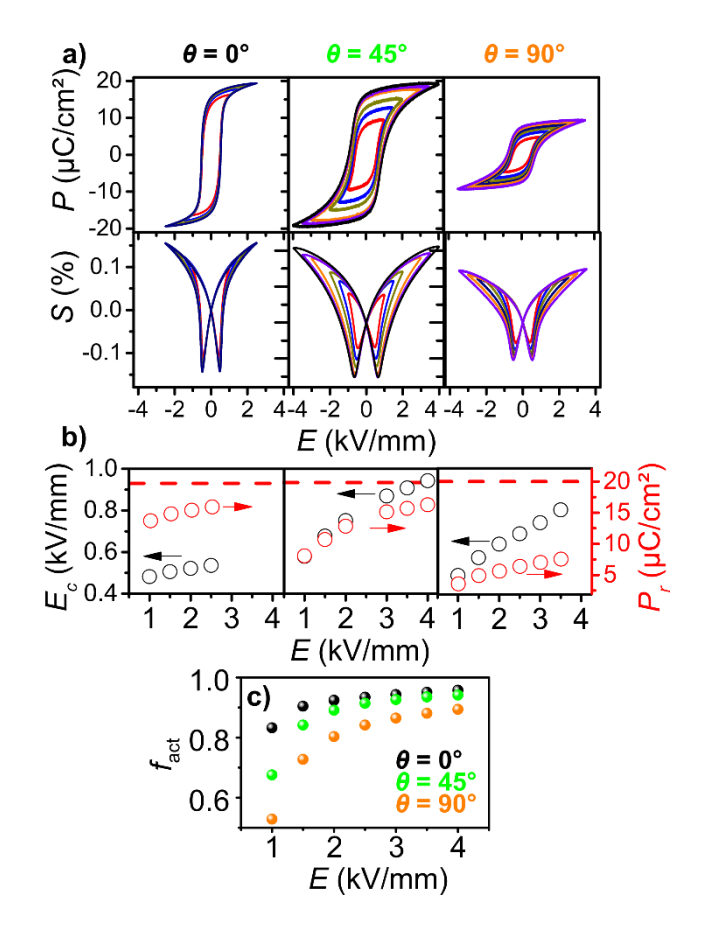


Figure 4: a) Field-dependent polarization and strain hysteresis loops for freeze cast samples with pores aligned at different angles  $\theta=0^\circ$ ,  $\theta=45^\circ$ , and  $\theta=90^\circ$  to the applied electric field. Field-dependent polarization and strain hysteresis loops for the dense counterpart are displayed in Figure S4 for comparison. b) Dependency of the coercive field and the remanent polarization on the amplitude of the applied electric field. Please note that these measurements were carried out on older samples, which explains the slight difference in the coercive field compared to parameters obtained on fresh samples, provided in Table 1. The dashed red lines represent the calculated remanent limiting polarization according to the porosity volume fraction,  $v_p$ , of a dense counterpart measured at 3.5 kV/mm (Equation 3, Figure S4). c) Field-dependence of the active fraction of material,  $f_{act}$ , obtained from the FE model (Figure 2).

# E. Switching dynamics

# a. Sequence of switching events

The results of the field-dependent measurements of the polarization switching behaviour for the investigated samples are displayed in Figure 5. The  $\Delta P(t)$  curves, presented in the upper row, exhibited the expected step-like behaviour [25]. The amount of switched polarization continuously decreased with increasing orientation angle of the anisometric pores. For example, under an applied electric field of  $E_{SW}=1.00 \, \mathrm{kV/mm}$ ,  $\Delta P_{E_{SW}=1.00 \, \mathrm{kV/mm}}^{\theta=0^{\circ}}(10s)=28.2 \, \mu \mathrm{C/cm^2}$  was reversed for the  $\theta=0^{\circ}$  sample, while only  $\Delta P_{E_{SW}=1.00 \, \mathrm{kV/mm}}^{\theta=90^{\circ}}(10s)=9.6 \, \mu \mathrm{C/cm^2}$  was reversed for the  $\theta=90^{\circ}$  sample.

The simultaneous measurements of S(t) are displayed in the second row of Figure 5. Three different regimes, as previously suggested [37], were identified based on the shape of the curves. The three regimes are numbered in Figure 5 for a selected HV pulse amplitude  $E_{Sw} = 0.55$  kV/mm. For samples with a pore orientation angle of  $\theta \ge 45^{\circ}$  it was not possible to observe the third regime within the investigated time interval of 10 s for HV pulse amplitudes  $E_{Sw} \le 0.55$  kV/mm due to the broadening of the switching response. Longer time intervals were avoided in this study due to initiation of electrical fatigue.

The impact of pore orientation angle  $\theta$  on the individual regimes of polarization reversal is displayed in Figure 6. Here,  $\Delta P(t)$  and S(t) curves for samples with different pore orientation angles  $\theta$  are compared for selected constant electric field pulses. The measurements of the dense sample are added for comparison. The impact of pore orientation angle on the first regime is plotted in Figure 6a (pulse amplitude  $E_{Sw}$  = 0.3 kV/mm). The slope  $\Delta S/\Delta \ln(t)$  is related to the dynamics/fraction of non-180° domain walls as previously derived for a dense tetragonal PZT model material using time resolved XRD experiments. [37,55] The slope was smallest for the sample with pores oriented perpendicular to the field and increased with decreasing  $\theta$ , approaching the value of the dense material. In addition, the amount of switched polarization  $\Delta P(10s)$  decreased with increasing pore orientation angle  $\theta$ . The transition between the first and the second switching regime (main switching phase) is displayed in Figure 6b (pulse amplitude  $E_{SW} = 0.5 \text{ kV/mm}$ ). This transition is defined by the changed sign of the slope  $\Delta S/\Delta \ln(t)$ . The transition is sharp for  $\theta=0^\circ$  samples, whereas the plateau broadens with increasing  $\theta$ . This observation is in good agreement with the bipolar strain loops presented in Figure 3b. Moreover, the maximum value of negative strain at the transition decreased with increasing  $\theta$ , as shown in Figure 6b. The second regime is displayed in more detail in Figure 6c (pulse amplitude  $E_{Sw} = 0.8 \text{ kV/mm}$ ). A

sharp increase of  $\Delta P(t)$ , quantified by the slope  $\partial(\Delta P)/\partial \ln(t)$  at the inflection point of the  $\Delta P(t)$  curves, was observed for  $\theta=0^\circ$ , while the slope decreased with increasing  $\theta$ . This indicates decreasing dynamics of the 180° switching events (nucleation and growth of 180° or non-180° domain walls) in the main switching phase [37] with increasing pore orientation angle.

# b. Activation fields for switching

The most important characteristic parameter of the main switching phase is the switching time,  $\tau$ , *i.e.*, the time at which the  $\Delta P(t)$  curves (Figure 5) inflect. Field-dependent switching times, obtained from Figure 5, are plotted as a function of the inverse  $E_{SW}$  in Figure 7a. The switching times increased with increasing pore orientation angle, which was related to the reduction of the amplitude of the local electric field due to porosity, demonstrated by the FE model (Figure 2). A physical correlation between  $\tau$  and  $E_{SW}$  is provided by the Merz law [56]:

$$\tau = \tau_0 \cdot \exp\left(\frac{E_a}{\kappa \cdot E_{SW}}\right)$$
 Equation 4

Here  $\tau_0$  is the characteristic switching time and  $E_a$  the activation field of the main switching phase. It is assumed that this activation field does not change for samples with different pore orientation angles, since the chemical composition and the mechanical boundary conditions (e.g., grain size, pore/ceramic channel width) remain unaffected. The reduction of the local electric field is taken into account by the factor  $\kappa$ . The dashed lines in Figure 7a represent fits according to Equation 4, whereby  $\kappa$  was used as a fitting parameter. The  $\theta=0^\circ$  sample was taken as reference, such that  $\kappa^{\theta=0^\circ}=1$ . The activation field of this sample was  $E_a^{\theta=0^\circ}=11.2\pm0.1\,\mathrm{kV/mm}$ . The dependence of the  $\kappa$  values on pore orientation angle is displayed in Figure 7b. The  $\kappa$  value decreased by 18% when the pores were rotated from  $\theta=0^\circ$  to  $\theta=90^\circ$ . The median local electric field determined from FE simulations (Figure 2b) is plotted for comparison in Figure 7b and it can be observed that the experimentally determined  $\kappa$  values display good qualitative agreement with the prediction of the theoretical model.

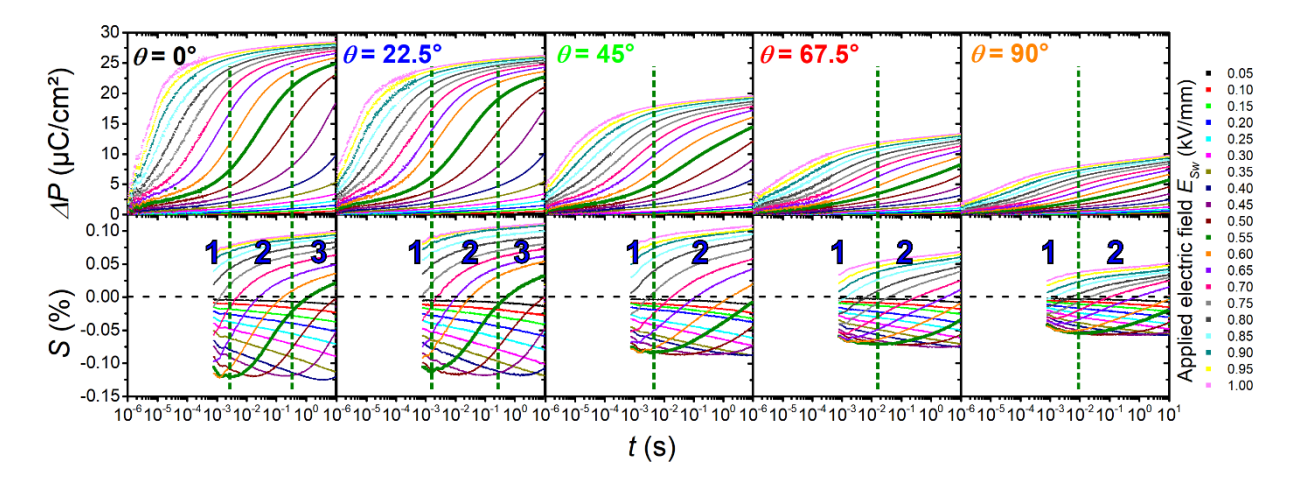


Figure 5: Simultaneous dynamic measurements of switched polarization,  $\Delta P(t)$ , and strain, S(t), of freeze cast porous PZT polycrystalline materials with anisometric pores aligned at different angles  $\theta$  to the external electric field. The curves were measured at different applied electric field pulses. The dashed horizontal black line represents zero relative strain, obtained by normalizing with the poled state. The numbers 1, 2, and 3 indicate the different regimes of polarization reversal (exemplarily shown for the  $E_{Sw} = 0.55$  kV/mm measurement), as previously suggested [37]. Due to the broadening of the switching behaviour, the third regime could not be observed for  $\theta \geq 45^\circ$  samples within the investigated time interval of 10 s for  $E_{Sw} \leq 0.55$  kV/mm.

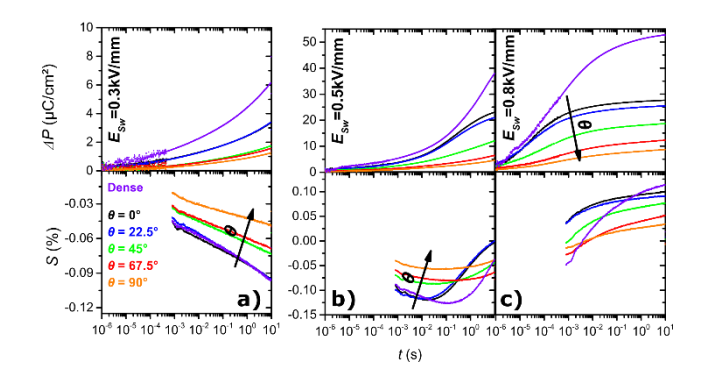


Figure 6: Selected  $\Delta P(t)$  and S(t) curves for constant electric fields,  $E_{Sw}$ . The influence of pore orientation angle on the shape of the  $\Delta P(t)$  and S(t) curves is displayed for a) non-180° domain wall movement (first regime), b) the transition between the first regime and the main switching phase (second regime), and c) the second regime. The arrows represent increasing pore orientation angle  $\theta$ .

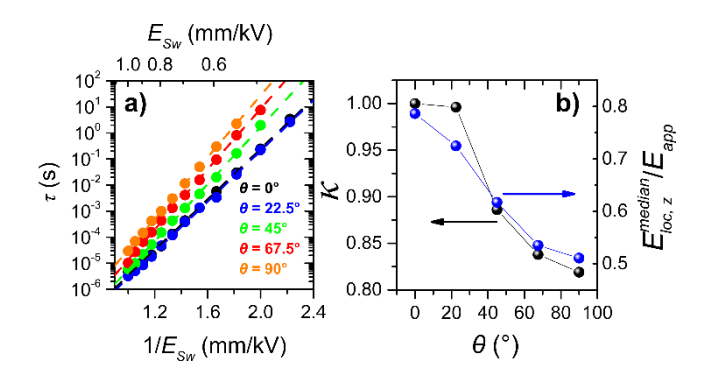


Figure 7: a) Field dependence of the characteristic switching time,  $\tau$ , of the main switching phase. The dashed lines represent fits according to the Merz law (Equation 4). b) Experimentally determined reduction of the local electric field, quantified by  $\kappa$  (Equation 4) for samples with anisometric pores oriented at different angles  $\theta$  to the external electric field. The normalized median z-component of the local electric field, determined from FE simulations (Figure 2b) is plotted for comparison.

## 4. Discussion

As outlined in the field- and time-dependent large signal measurements, the orientation of anisometric pores with respect to the applied electric field direction considerably impacts the polarization reversal. The main origin of this behaviour is the decrease of the local electric field with increasing pore orientation angle. FE simulations of the local distribution of the externally applied field in the investigated materials display a shifting by 35% towards lower values for increasing pore angle (see Figure 2b), which is in good qualitative agreement to previous calculations [26,28,29,57]. Experimentally, the impact of the pore orientation was quantified by two factors ( $d_P$  and  $\kappa$ ), which are related to the distribution of the local electric field. While the depolarization factor ( $d_P$ ) physically quantifies the fraction of active material, the factor  $\kappa$  accounts for the interplay between polarization reversal and the applied electric field in the active material. These two aspects will be discussed in the following section.

## A. Active material

The volume fraction of the active material decreases with increasing pore angle. This can be quantified by the decreasing negative strain at the transition between regimes 1 and 2 (Figure 6b), the lower value of switched polarization  $\Delta P_{E_{SW}}^{\theta}(10s)$  (Figure 6a), and the decreased remanent polarization (Table 1). As outlined in Figure 4, the

reduction in remanent polarization and strain with increasing pore angle can be overcome if the amplitude of the external electric field is increased. This was demonstrated for the  $\theta=45^\circ$  sample, where the remanent polarization was doubled when the electric field was increased from 1.0 kV/mm to 4.0 kV/mm. This finding is in agreement to previous investigations where a dependence of remanent polarization on the applied electric field was observed for freeze cast samples with pores aligned parallel and perpendicular to the electric field. [10] Interestingly, both non-180° and 180° switching events are affected, as the maximum negative strain and the squareness of the loops both increase with increasing electric field (Figure 4a). Considering the local electric field (Figure 2), an increase of the applied field results in a shift of the local field to higher absolute values, triggering switching in previously low field regions (quantified in Figure 4c). The good agreement between the experimental and modelling results confirms that the field-dependency of the remanent polarization is related to the decrease and broadening of local electric field amplitudes, caused by the variation of orientation angle of the anisometric pores.

The depolarization factor (Equation 3) quantifies the volume fraction of active material within a porous ferroelectric. In a previous investigation into Ni<sub>0.4</sub>Zn<sub>0.6</sub>Fe<sub>2</sub>O<sub>4</sub> polycrystalline ceramics it was suggested that a  $d_P \leq 1$  is required in order to describe the porosity dependence of the permeability of these materials [58]. Later on, this approach was transferred to ferroelectric PZT polycrystalline ceramics [54]. Physically, the depolarization factor reduces the effective remanent polarization of a porous material by taking into account the volume of high permittivity material surrounding a pore that is subject to a comparably lower field than the applied external field [32]. Based on experimental results [59,60], it was suggested that the depolarization factor depends on the type of porosity. On the one hand, the depolarization factor was found to be dependent on the volume fraction of porosity and the orientation angle of anisometric pores with respect to the electric field, however, it was found that pore size had little impact [61]. Interestingly, these findings reflect the distribution of the local electric field due to presence of porosity. While the distribution of the local electric field was found to be affected by the volume fraction of porosity and the orientation angle of anisometric pores with respect to the electric field, it remained unaffected by the size of the pores [26]. Here, we have demonstrated that the depolarization factor is correlated to the local distribution of the electric field and a higher fraction of material can be activated if the externally applied field is increased. This finding offers the possibility of tailoring the remanent polarization and strain with the applied electric field and the microstructure.

#### B. Domain wall movement

Domain wall movement in ferroelectrics is influenced by multiple parameters, including the crystal structure, chemical composition, grain boundaries, and the local electric field distributions. In porous ferroelectrics, the influence of the latter one is particularly important. For example, the dynamics of non-180° domain walls in regime 1 (Figure 6a) and the switching times of the main switching phase (Figure 6c, Figure 7a) decrease with increasing pore angle. Please note that in the main switching phase 180° switching events or synchronized non-180° switching events are active, as discussed elsewhere. [37,38] A decreased dynamic also results in a broadening of the switching behaviour, as evidenced by the decrease of the squareness ratio (Table 1, Figure 3) and by the broadening of the transition between regimes 1 and 2 (Figure 6b). These results can be explained by the locally reduced electric field in porous samples with increasing pore orientation angle (Figure 2). Switching dynamic measurements outline that the factor  $\kappa$ , which experimentally quantifies the reduction of the externally applied electric field, was reduced by 18% for the  $\theta = 90^{\circ}$  compared to the  $\theta = 0^{\circ}$ sample. As revealed by FE simulations in Figure 2b, the reduction of the local electric field is a direct consequence of the orientation of the anisometric pores with respect to the electric field. The correlation between the factor  $\kappa$  and the median local electric field is displayed in Figure 7b. The influence of the local electric field on the domain wall dynamics is a well-investigated phenomenon in BaTiO<sub>3</sub> single crystals. In seminal studies [62-64], it was outlined that the dynamics of domain walls decreases with decreasing field amplitude. A facile obtainable parameter, which is commonly used to quantify the easiness of domain wall movement, is the coercive field, which is discussed in the context of porous materials below.

## Coercive field of porous materials

As outlined in Figure 4a and b, increasing the active material fraction is accompanied by an increase in the coercive field. For example, the coercive field rises by 65% if the applied electric field is changed from 1.0 kV/mm to 4.0 kV/mm for the  $\theta=45^{\circ}$  sample. In comparison, the coercive field remains nearly unaffected for the  $\theta=0^{\circ}$  sample. Ideally, the coercive field is obtained from a saturated polarization loop, which switches

the entire polarization of the sample. However, in porous materials this condition is experimentally difficult to obtain, since electric breakdown of the sample usually occurs before the entire polarization of the sample has been reversed. It should be noted that the dependence of the coercive field on the applied field is much less pronounced for dense materials, for which the distribution of the local electric field is sharp around the applied electric field (see Figures 2c and S4).

A consequence of this finding is that a direct comparison of coercive fields obtained from polarization measurements of porous materials should be undertaken with care. This may shed light on the previously revealed discrepancy regarding the impact of porosity on the ease of polarization reversal [32]. While some authors claimed that the coercive field decreases with increasing total porosity [27,65], others found an increase [33,54] or even no effect [66,67]. Some have reported that the coercive field is first decreasing and subsequently increasing [10,32]. In contrast, theoretical approaches, i.e. by Wersing et al. [68] or Banno [69], predict a dramatic increase of the coercive field with increasing total porosity, without providing a deeper discussion of the underlying processes. In the framework of the materials investigated in this work, it was found that the coercive field increased with increasing pore orientation angle (Table 1, Figure 4a and b). This increase represents the compensation of the shift of the local electric field distributions to lower values, which is most pronounced for materials with a large pore orientation angle. The coercive field of porous materials should thus not be considered as reflecting the ease of domain wall motion, since it is strongly influenced by the local field distribution. In fact, the domain wall motion might be even facilitated in porous materials due to changed mechanical boundary conditions, as previously suggested for thin films [70] and discussed in the following paragraph.

#### Mechanical boundary conditions

The activation field for polarization reversal of the dense material was found to be comparable to the one of the porous PZT with a pore orientation of  $\theta=0^\circ$  ( $E_a^{dense}=11.4\pm0.2\,\text{kV/mm}$ ) with a  $\kappa$  value of 1 used in both cases. However, we note that a smaller activation field would be obtained for the  $\theta=0^\circ$  sample (8.7 kV/mm, using  $\kappa=0.78$  in Equation 4) if the 22% difference between the median fields of the  $\theta=0^\circ$  sample and the dense sample were taken into account, as obtained from FE simulations (Figure 2b and c). The difference in the activation fields between the dense

and the porous sample indicates easier polarization reversal in the porous materials, possibly due to different mechanical boundary conditions in the vicinity of the pores compared with the dense counterpart. Enhanced domain switching fraction of ferroelectric/ferroelastic domains in porous films, as compared to their dense counterparts, has been previously observed [70,71] and was related to substrate declamping effects [72,73]. However, more detailed investigations using advanced diffraction techniques are required in bulk porous materials to fully understand, and potentially utilize, this behaviour in the future.

#### 5. Conclusion

Porous polycrystalline lead zirconate titanate samples were investigated to understand the relationships between ferroelectric/ferroelastic switching, local electric field distributions, and resultant functional properties. The porous samples were freeze cast to obtain highly anisometric pore morphologies oriented at varying angles respective to applied electric fields. Using detailed finite element simulations, it was calculated that the distribution of the local electric field was shifted towards lower values when the pores were oriented perpendicular to the applied electric field. The highest piezoelectric strain coefficient in the porous material,  $d_{33} = 630$  pm/V, was achieved when pores were aligned with the poling direction, which was comparable to the dense value ( $d_{33} = 648 \text{ pm/V}$ ). On the other hand, the porous sample with pores oriented perpendicular to the poling direction exhibited the highest figures of merit,  $g_{33}=216$  $10^{-3}$  Vm/N and  $d_{33}g_{33}=73\cdot 10^{-12}$  m²/N, which were 12 and 6 times higher than the respective figures of merit for the dense material, due to significant reductions in the effective permittivity. These small signal figures of merits demonstrate the feasibility of porous materials for piezoelectric energy harvesters, hydrophones, or medical ultrasound devices. In addition, large signal strain loops of samples with pores oriented parallel to the electric field exhibit similar macroscopic strain behaviour compared to dense PZT, indicating the possibility of using these lower density materials as lowforce actuators or transmitters.

The polarization reversal behaviour of the material was investigated by time-dependent simultaneous measurements of polarization and strain. A modified version of the Merz law was used to quantify the decrease in the external applied switching field due to the

porous microstructure of the material. The local electric field for polarization reversal was found to be reduced when the pore orientation angle increased. Consequently, the dynamics of the domains decreased and the distribution of switching times broadened. In addition, the shape, coercive field, and remanent polarization were found to be impacted by the applied electric field amplitude during bipolar cycling, which is a direct consequence of the distribution of the electric field within the porous materials. The observed experimental results were explained in the frame of the difference in the local electric field caused by the microstructure of the porous materials, which were simulated by a two-dimensional finite element model with good agreement to experimental data. A detailed understanding of the interplay between the electric field and polarization reversal was shown to be critical for the accurate interpretation of measurements on porous ferroelectric materials. Tailoring the poling conditions through time and applied field offers the possibility to further enhance the longitudinal piezoelectric coefficient and thus to tailor the respective figures of merit for applications.

# **Acknowledgements**

This work was supported by the Deutsche Forschungsgemeinschaft (DFG), Grant No. KO 5100/1-1 (270195408). C. R. Bowen, R. Khachaturyan, and Y. Genenko are acknowledged for valuable discussions and helpful input.

#### References

- [1] Q. Y. Jiang and L. E. Cross, Effects of Porosity on Electric Fatigue Behavior in PLZT and PZT Ferroelectric Ceramics, J. Mater. Sci. **28**, 4536 (1993).
- [2] S. Meille, M. Lombardi, J. Chevalier, and L. Montanaro, Mechanical properties of porous ceramics in compression: On the transition between elastic, brittle, and cellular behavior, J. Eur. Ceram. Soc. **32**, 3959 (2012).
- [3] C. Galassi, Processing of porous ceramics: Piezoelectric materials, J. Eur. Ceram. Soc. **26**, 2951 (2006).
- [4] D. P. Skinner, R. E. Newnham, and L. E. Cross, Flexible Composite Transducers, Mater. Res. Bull. **13**, 599 (1978).
- [5] S. Marselli, V. Pavia, C. Galassi, E. Roncari, F. Craciun, and G. Guidarelli, Porous piezoelectric ceramic hydrophone, J. Acoust. Soc. Am. **106**, 733 (1999).
- [6] H. Kara, R. Ramesh, R. Stevens, and C. R. Bowen, Porous PZT ceramics for receiving transducers, IEEE T. Ultrason. Ferr. **50**, 289 (2003).
- [7] A. K. Yang, C. A. Wang, R. Guo, Y. Huang, and C. W. Nan, Porous PZT Ceramics with High Hydrostatic Figure of Merit and Low Acoustic Impedance by TBA-Based Gel-Casting Process, J. Am. Ceram. Soc. **93**, 1427 (2010).
- [8] C. P. Shaw, R. W. Whatmore, and J. R. Alcock, Porous, functionally gradient pyroelectric materials, J. Am. Ceram. Soc. **90**, 137 (2007).
- [9] S. B. Lang and E. Ringgaard, Measurements of the thermal, dielectric, piezoelectric, pyroelectric and elastic properties of porous PZT samples, Appl. Phys. A **107**, 631 (2012).
- [10] Y. Zhang, M. Xie, J. Roscow, Y. Bao, K. Zhou, D. Zhang, and C. R. Bowen, Enhanced pyroelectric and piezoelectric properties of PZT with aligned porosity for energy harvesting applications, J. Mater. Chem. A **5**, 6569 (2017).
- [11] J. I. Roscow, R. W. C. Lewis, J. Taylor, and C. R. Bowen, Modelling and fabrication of porous sandwich layer barium titanate with improved piezoelectric energy harvesting figures of merit, Acta Mater. **128**, 207 (2017).
- [12] J. I. Roscow, Y. Zhang, M. J. Krasny, R. W. C. Lewis, J. Taylor, and C. R. Bowen, Freeze cast porous barium titanate for enhanced piezoelectric energy harvesting, J. Phys. D: Appl. Phys. **51**, 225301 (2018).
- [13] R. Guo, C. A. Wang, and A. K. Yang, Effects of pore size and orientation on dielectric and piezoelectric properties of 1-3 type porous PZT ceramics, J. Eur. Ceram. Soc. **31**, 605 (2011).
- [14] K. Rittenmyer, T. Shrout, W. A. Schulze, and R. E. Newnham, Piezoelectric 3–3 composites, Ferroelectrics **41**, 189 (1982).
- [15] S. H. Lee, S. H. Jun, H. E. Kim, and Y. H. Koh, Piezoelectric Properties of PZT Based Ceramic with Highly Aligned Pores, J. Am. Ceram. Soc. **91**, 1912 (2008).
- [16] S. H. Lee, S. H. Jun, H. E. Kim, and Y. H. Koh, Fabrication of porous PZT-PZN piezoelectric ceramics with high hydrostatic figure of merits using camphene-based freeze casting, J. Am. Ceram. Soc. **90**, 2807 (2007).
- [17] R. E. Newnham, D. P. Skinner, and L. E. Cross, Connectivity and Piezoelectric-Pyroelectric Composites, Mater. Res. Bull. **13**, 525 (1978).
- [18] S. Priya, Criterion for Material Selection in Design of Bulk Piezoelectric Energy Harvesters, IEEE T. Ultrason. Ferr. **57**, 2610 (2010).
- [19] C. W. Bert, Prediction of Elastic-Moduli of Solids with Oriented Porosity, J. Mater. Sci. **20**, 2220 (1985).
- [20] S. Deville, Freeze-Casting of Porous Biomaterials: Structure, Properties and Opportunities, Materials **3**, 1913 (2010).
- [21] K. Uchino, Piezoelectric Energy Harvesting Systems-Essentials to Successful Developments, Energy Technol. **6**, 829 (2018).
- [22] J. Seuba, S. Deville, C. Guizard, and A. J. Stevenson, Mechanical properties and failure behavior of unidirectional porous ceramics, Sci. Rep. **6** (2016).

- [23] A. Boccaccini, G. Ondracek, P. Mazilu, and D. Windelberg, On the effective Young's modulus of elasticity for porous materials: microstructure modelling and comparison between calculated and experimental values, J. Mech. Behav. Mater. **4**, 119 (1993).
- [24] D. C. Lupascu, S. Fedosov, C. Verdier, J. Rödel, and H. von Seggern, Stretched exponential relaxation in perovskite ferroelectrics after cyclic loading, J. Appl. Phys. **95**, 1386 (2004).
- [25] Y. A. Genenko, S. Zhukov, S. V. Yampolskii, J. Schütrumpf, R. Dittmer, W. Jo, H. Kungl, M. J. Hoffmann, and H. von Seggern, Universal Polarization Switching Behavior of Disordered Ferroelectrics, Adv. Funct. Mater. **22**, 2058 (2012).
- [26] R. Khachaturyan, S. Zhukov, J. Schultheiß, C. Galassi, C. Reimuth, J. Koruza, H. von Seggern, and Y. A. Genenko, Polarization-switching dynamics in bulk ferroelectrics with isometric and oriented anisometric pores, J. Phys. D: Appl. Phys. **50**, 045303 (2017).
- [27] F. Gheorghiu, L. Padurariu, M. Airimioaei, L. Curecheriu, C. Ciomaga, C. Padurariu, C. Galassi, and L. Mitoseriu, Porosity-dependent properties of Nb-doped Pb(Zr,Ti)O<sub>3</sub> ceramics, J. Am. Ceram. Soc. **100**, 647 (2017).
- [28] L. Padurariu, L. P. Curecheriu, and L. Mitoseriu, Nonlinear dielectric properties of paraelectric-dielectric composites described by a 3D Finite Element Method based on Landau-Devonshire theory, Acta Mater. **103**, 724 (2016).
- [29] L. Padurariu, L. Curecheriu, C. Galassi, and L. Mitoseriu, Tailoring non-linear dielectric properties by local field engineering in anisotropic porous ferroelectric structures, Appl. Phys. Lett. **100**, 252905 (2012).
- [30] L. Stoleriu, A. Stancu, L. Mitoseriu, D. Piazza, and C. Galassi, Analysis of switching properties of porous ferroelectric ceramics by means of first-order reversal curve diagrams, Phys. Rev. B **74**, 174107 (2006).
- [31] D. Piazza, L. Stoleriu, L. Mitoseriu, A. Stancu, and C. Galassi, Characterisation of porous PZT ceramics by first-order reversal curves (FORC) diagrams, J. Eur. Ceram. Soc. **26**, 2959 (2006).
- [32] Y. Zhang, J. Roscow, R. Lewis, H. Khanbareh, V. Y. Topolov, M. Y. Xie, and C. R. Bowen, Understanding the effect of porosity on the polarisation-field response of ferroelectric materials, Acta Mater. **154**, 100 (2018).
- [33] E. Barabanova, O. Malyshkina, A. Ivanova, E. Posadova, K. Zaborovskiy, and A. Daineko, in *IOP Conference Series: Materials Science and Engineering* (IOP Publishing, 2013), p. 012026.
- [34] T. Bakarič, T. Rojac, A. P. Abellard, B. Malič, F. Levassort, and D. Kuscer, Effect of pore size and porosity on piezoelectric and acoustic properties of Pb(Zr<sub>0.53</sub>Ti<sub>0.47</sub>)O<sub>3</sub> ceramics, Adv. Appl. Ceram. **115**. 66 (2016).
- [35] C. A. Randall, N. Kim, J. P. Kucera, W. W. Cao, and T. R. Shrout, Intrinsic and extrinsic size effects in fine-grained morphotropic-phase-boundary lead zirconate titanate ceramics, J. Am. Ceram. Soc. **81**, 677 (1998).
- [36] L. Jin, F. Li, and S. J. Zhang, Decoding the Fingerprint of Ferroelectric Loops: Comprehension of the Material Properties and Structures, J. Am. Ceram. Soc. **97**, 1 (2014).
- [37] J. Schultheiß, L. Liu, H. Kungl, M. Weber, L. Kodumudi Venkataraman, S. Checchia, D. Damjanovic, J. E. Daniels, and J. Koruza, Revealing the sequence of switching mechanisms in polycrystalline ferroelectric/ferroelastic materials, Acta Mater. **157**, 355 (2018).
- [38] Y. A. Genenko, R. Khachaturyan, J. Schultheiß, A. Ossipov, J. E. Daniels, and J. Koruza, Stochastic multistep polarization switching in ferroelectrics, Phys. Rev. B **97**, 144101 (2018).
- [39] E. T. Keve and K. L. Bye, Phase Identification and Domain-Structure in PLZT Ceramics, J. Appl. Phys. **46**, 810 (1975).
- [40] P. Gerthsen and G. Krüger, Coercive Field in Fine-Grained PLZT Ceramics, Ferroelectrics **11**, 489 (1976).
- [41] J. E. Daniels, C. Cozzan, S. Ukritnukun, G. Tutuncu, J. Andrieux, J. Glaum, C. Dosch, W. Jo, and J. L. Jones, Two-step polarization reversal in biased ferroelectrics, J. Appl. Phys. **115**, 224104 (2014).
- [42] W. Wersing, Hystereseeigenschaften ferroelektrischer Keramiken, Ber. Dtsch. Keram. Ges. **51**, 318 (1974).

- [43] G. Arlt, A model for switching and hysteresis in ferroelectric ceramics, Integr. Ferroelectr. **16**, 229 (1997).
- [44] G. Viola, K. B. Chong, F. Guiu, and M. J. Reece, Role of internal field and exhaustion in ferroelectric switching, J. Appl. Phys. **115**, 034106 (2014).
- [45] J. Schultheiß, H. Kungl, and J. Koruza, Influence of crystallographic structure on polarization reversal in polycrystalline ferroelectric/ferroelastic materials, J. Appl. Phys. **125**, 174101 (2019).
- [46] M. I. Mendelson, Average Grain Size in Polycrystalline Ceramics, J. Am. Ceram. Soc. **52**, 443 (1969).
- [47] H. von Seggern and S. Fedosov, A novel displacement component in PVDF and its role in ferroelectric switching, IEEE Trans. Dielectr. Electr. Insul. **7**, 543 (2000).
- [48] C. Sakaki, B. L. Newalkar, S. Komarneni, and K. Uchino, Grain size dependence of high power piezoelectric characteristics in Nb doped lead zirconate titanate oxide ceramics, Jpn. J. Appl. Phys. **40**, 6907 (2001).
- [49] G. Arlt, Twinning in Ferroelectric and Ferroelastic Ceramics Stress Relief, J. Mater. Sci. **25**, 2655 (1990).
- [50] R. Khachaturyan and Y. A. Genenko, Correlated polarization-switching kinetics in bulk polycrystalline ferroelectrics. II. Impact of crystalline phase symmetries, Phys. Rev. B **98**, 134106 (2018).
- [51] K. G. Webber, D. J. Franzbach, and J. Koruza, Determination of the True Operational Range of a Piezoelectric Actuator, J. Am. Ceram. Soc. **97**, 2842 (2014).
- [52] F. Mohammadi, A. Kholkin, B. Jadidian, and A. Safari, High-displacement spiral piezoelectric actuators, Appl. Phys. Lett. **75**, 2488 (1999).
- [53] G. Haertling and W. Zimmer, An Analysis of Hot-Pressing Parameters for Lead Zirconate-Lead Titanate Ceramics containing 2 Atom Percent Bismuth, Am. Ceram. Soc. Bull. **45**, 1084 (1966).
- [54] K. Nagata, Effects of porosity and grain size on hysteresis loops of piezoelectric ceramics (PbLa)(ZrTi)O<sub>3</sub>, Electr. Eng. Jpn. **100**, 1 (1980).
- [55] D. A. Hall, A. Steuwer, B. Cherdhirunkorn, T. Mori, and P. J. Withers, A high energy synchrotron x-ray study of crystallographic texture and lattice strain in soft lead zirconate titanate ceramics, J. Appl. Phys. **96**, 4245 (2004).
- [56] W. J. Merz, Domain Formation and Domain Wall Motions in Ferroelectric BaTiO₃ Single Crystals, Phys. Rev. **95**, 690 (1954).
- [57] C. S. Olariu, L. Padurariu, R. Stanculescu, C. Baldisserri, C. Galassi, and L. Mitoseriu, Investigation of low field dielectric properties of anisotropic porous Pb(Zr,Ti)O<sub>3</sub> ceramics: Experiment and modeling, J. Appl. Phys. **114**, 214101 (2013).
- [58] H. Igarashi and K. Okazaki, Effects of Porosity and Grain-Size on Magnetic-Properties of NiZn Ferrite, J. Am. Ceram. Soc. **60**, 51 (1977).
- [59] H. Igarashi, S. Tashiro, and K. Okazaki, Depolarization factor of dielectric ceramics including pores, Mem. Nat. Defense Acad. **19**, 87 (1979).
- [60] K. Okazaki and H. Igarashi, *Importance of microstructure in electronic ceramics* (1976), Vol. 76, Ceramic Microstructure.
- [61] K. Okazaki, Recent Developments in Piezoelectric Ceramics in Japan, Ferroelectrics **35**, 173 (1981).
- [62] R. C. Miller and A. Savage, Velocity of Sidewise 180° Domain-Wall Motion in BaTiO<sub>3</sub> as a Function of the Applied Electric Field, Phys. Rev. **112**, 755 (1958).
- [63] H. L. Stadler, Forward Velocity of 180° Ferroelectric Domain Walls in BaTiO<sub>3</sub>, J. Appl. Phys. **37**, 1947 (1966).
- [64] G. W. Taylor, High Field Polarization Reversals in Liquid Electroded Barium Titanate Crystals, Aust. J. Phys. **15**, 549 (1962).
- [65] H. L. Zhang, J. F. Li, and B. P. Zhang, Microstructure and electrical properties of porous PZT ceramics derived from different pore-forming agents, Acta Mater. **55**, 171 (2007).

- [66] E. W. Yap, J. Glaum, J. Oddershede, and J. E. Daniels, Effect of porosity on the ferroelectric and piezoelectric properties of (Ba<sub>0.85</sub>Ca<sub>0.15</sub>)(Zr<sub>0.1</sub>Ti<sub>0.9</sub>)O<sub>3</sub> piezoelectric ceramics, Scr. Mater. **145**, 122 (2018).
- [67] S. Geis, J. Fricke, and P. Löbmann, Electrical properties of PZT aerogels, J. Eur. Ceram. Soc. **22**, 1155 (2002).
- [68] W. Wersing, K. Lubitz, and J. Mohaupt, Dielectric, elastic and piezoelectric properties of porous PZT ceramics, Ferroelectrics **68**, 77 (1986).
- [69] H. Banno, Effects of Shape and Volume Fraction of Closed Pores on Remanent Polarization and Coercive Force of Ferroelectric Ceramics, Jpn. J. Appl. Phys. **26**, 50 (1987).
- [70] R. L. Johnson-Wilke, R. H. T. Wilke, M. Wallace, A. Rajashekhar, G. Esteves, Z. Merritt, J. L. Jones, and S. Trolier-McKinstry, Ferroelectric/Ferroelastic Domain Wall Motion in Dense and Porous Tetragonal Lead Zirconate Titanate Films, IEEE T. Ultrason. Ferr. **62**, 46 (2015).
- [71] A. Matavž, A. Bradeško, T. Rojac, B. Malič, and V. Bobnar, Self-assembled porous ferroelectric thin films with a greatly enhanced piezoelectric response, Appl. Mater. Today **16**, 83 (2019).
- [72] F. Griggio, S. Jesse, A. Kumar, O. Ovchinnikov, H. Kim, T. N. Jackson, D. Damjanovic, S. V. Kalinin, and S. Trolier-McKinstry, Substrate Clamping Effects on Irreversible Domain Wall Dynamics in Lead Zirconate Titanate Thin Films, Phys. Rev. Lett. **108**, 157604 (2012).
- [73] L. M. Denis, G. Esteves, J. Walker, J. L. Jones, and S. Trolier-McKinstry, Thickness dependent response of domain wall motion in declamped  $\{001\}$  Pb $\{Zr_{0.3}Ti_{0.7}\}O_3$  thin films, Acta Mater. **151**, 243 (2018).